Physics of Fluids

RESEARCH ARTICLE | APRIL 26 2023

Gender in human phonation: Fluid–structure interaction and vocal fold morphology

Isabella McCollum; Alexis Throop; Durwash Badr; ... et. al

Physics of Fluids 35, 041907 (2023)
https://doi.org/10.1063/5.0146162

Physics of Fluids ARTICLE scitation.org/journal/phf

Gender in human phonation: Fluid–structure interaction and vocal fold morphology

Cite as: Phys. Fluids **35**, 041907 (2023); doi: 10.1063/5.0146162
Submitted: 10 February 2023 · Accepted: 12 April 2023 ·
Published Online: 26 April 2023

View Online Export Citation CrossMark

Isabella McCollum, Alexis Throop, Durwash Badr, and Rana Zakerzadeh[a)]

AFFILIATIONS

Department of Engineering, Rangos School of Health Sciences, Duquesne University, Pittsburgh, Pennsylvania 15219, USA

[a)]Author to whom correspondence should be addressed: zakerzadehr@duq.edu

ABSTRACT

This paper aims to examine the effects of variations in the vocal fold (VF) morphological features associated with gender on glottal aerodynamics and tissue deformation. Nine three-dimensional geometries of the VFs in the larynx are created with various VF lengths, thicknesses, and depths to perform a parametric analysis according to gender-related geometrical parameters. The computational model is incorporated in a fluid–structure interaction methodology by adopting the transient Navier–Stokes equations to model airflow through the larynx and considering a linear elasticity model for VF dynamics. The model predictions, such as aerodynamic data through the larynx, glottal airflow, and VF deformations, are analyzed. The comparison of the simulation results for the nine cases supports the hypothesis that gender differences in laryngeal dimensions remarkably influence the glottal airflow and deformation of the VFs. Decreasing VF thickness and increasing its length corresponds to a noticeable increase in maximum tissue displacement, while variations in depth affect the flow rate significantly in the small and large larynges. Conversely, we observed that the pressure drop at the glottis is nearly independent of the VF length. A comparison of the glottal area with published imaging data illustrated a direct correlation between the glottal configuration and the morphology of the VFs.

I. INTRODUCTION

The human phonation process involves fluid–structure interactions (FSIs) of airflow in the larynx and the flow-induced vibrations of the vocal fold (VF) tissue.[1] An improved understanding of these interactions is useful for studying VF pathology and the physics of voice,[1] enhancement in the prevention of voice disorders,[2] and developing computer-based tools for their clinical management.[3]

Clinical studies have observed that male and female larynges differ in their geometrical characteristics, which are correlated with differences in VF vibratory patterns between the two genders.[4] In particular, it has been found that males have longer, thicker VFs that are placed in a larger larynx, while females on average have VFs that are 60% shorter anteriorly posteriorly and 20%–30% thinner along the vertical direction than male VFs,[5] as well as the smaller larynx (Fig. 1). Due to these gender-related anatomical variations, the fundamental speaking frequency of females is about two times higher than males,[6] which can contribute to a higher prevalence of certain voice disorders in one gender.[7] Statistically, women have been found to experience VF lesions more frequently than men, regardless of their occupation.[8] This disproportion can partially be explained by different geometries of the laryngeal framework for females and males, and corresponding VF dimensions.[8,9] It has been hypothesized that shorter VFs experience more oscillations and collisions for an equal amount of voicing, while there would be less tissue to absorb vibratory forces in a thinner VF tissue.[4,10]

Analyzing the relationship between VF morphological properties and function in phonation leads to improvements in biomechanical models of the human larynx, while such models are also being considered for potential use in surgical interventions[11] and the design of laryngeal prostheses,[12] as well as exploring issues related to gender and voice training.[13,14] Previous studies have observed the size ranges of the human VFs but very few research has attempted to explore the implication of differences in the structural dimensions on the phonation process and functional patterns; consequently, it is not clear to what extent the exclusion of geometrical variations modifies the VF and glottal flow dynamics and the effects of the size of the VFs remain uncertain.

Current efforts to develop computational models of voice production are critically reviewed in Ref. 16, including models to study changes in aerodynamics during VF vibration[17,18] and FSI studies of VF.[19–24] However, there are very few published reports that compare the phonation process and VF function according to female and male

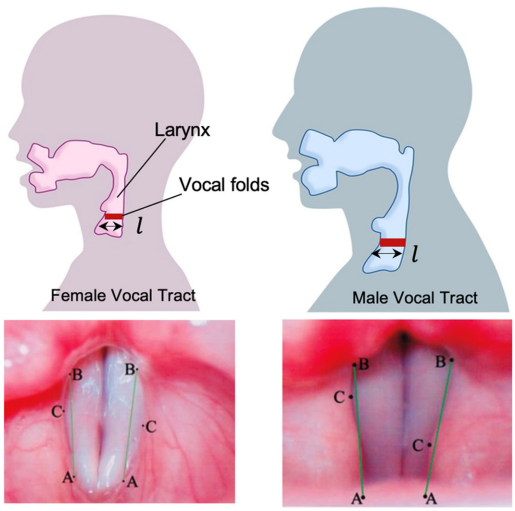

FIG. 1. Top: schematic of the human vocal tract system demonstrating gender differences. Bottom: a laryngeal image of female and male VFs from the superior view adapted from Nemetz *et al.*, Rev. Bras. Otorrinolaringol. **71**, 6–12 (2005).[15] Copyright 2005 licensed under a Creative Commons Attribution (CC BY) license, the straight-line AB represents the length of the folds.

geometry of the human larynx. Those that do exist employed a range of simplifications and limitations such as ignoring glottal aerodynamics in the larynx and inducing the vibration by applying direct load pressures to the VF surfaces, conducting pure fluid flow simulations by neglecting structural vibration of the tissue, considering only one VF based on symmetry assumption, and using lower dimensional models. Döllinger *et al.*[25] attempted to correlate anatomical parameters of VF to aerodynamics by adapting a two-mass mathematical model that expressed the gender-related differences indirectly by computed biomechanical model parameters. Other gender-related computational studies on VF biomechanical features have been conducted by Zhang.[26] and Li *et al.*,[27] which fail to simulate the realistic physics of phonation due to neglecting the fully coupled behavior of airflow and VF tissue. Li *et al.*[27] employed computational fluid mechanics (CFD) to demonstrate the differences in shape and size of the male and female larynxes such as glottal angles and the related transglottal pressure distributions, but without including the VF structural mechanics. Moreover, Zhang.[26] investigated the effects of differences in VF length, thickness, and depth on voice production via a reduced-order phonation model that considers glottal flow as a one-dimensional quasi-steady potential flow and the VF displacement is approximated using its precalculated eigenmodes, derived from Lagrange's equation. Furthermore, subglottal and supraglottal tracts were excluded in the aforementioned study, although their interaction with the glottal flow needs to be investigated.

Although the above studies were found to suggest significant attribution of larynx and VF morphological features, no previous research has attempted to explore the effects on dynamics of the glottal flow and VF deformations using an integrated FSI methodology capable of simulating the complex interactions present in this coupled system. The present effort attempts to remedy this deficit. More precisely, the objective of this study is to implement a physiologically realistic model of coupled glottal flow and VF vibration during phonation for the purpose of evaluating the influence of the VFs geometric parameters and analyzing the association of different morphological features with aerodynamics through the larynx and VF tissue deformation. A parametric study using comparative analysis of nine laryngeal models with various geometrical features is performed.

This paper is organized as follows: Sec. II reviews the formulation of the problem, introduces the parametric geometrical space and nine adopted VF models and summarizes the computational setup to perform the simulations. The computational results on aerodynamic data and tissue deformation are compared for simulated VF cases in Sec. III. Finally, the discussion, conclusions, and future directions are presented in Sec. IV.

II. METHODS

A three-dimensional (3D) model of the larynx containing VFs is considered (Fig. 2). The rectangular channel represents the air domain and is divided into subglottal, supraglottal, and glottal regions. The sub- and supraglottal lengths are selected based on experimental results[28] to capture the whole glottal flow. The flow direction is along the axial midline, and the computational domain is assumed to be symmetric about the glottal channel centerline.

The VFs, which are shown in red (Fig. 2), the glottis, and the shapes of the false VFs comprise the glottal space. Using the laryngeal CT scan of a human subject, obtained from Ref. 24 and demonstrated in Fig. 2(a), the cross-sectional geometry of the baseline VF model is

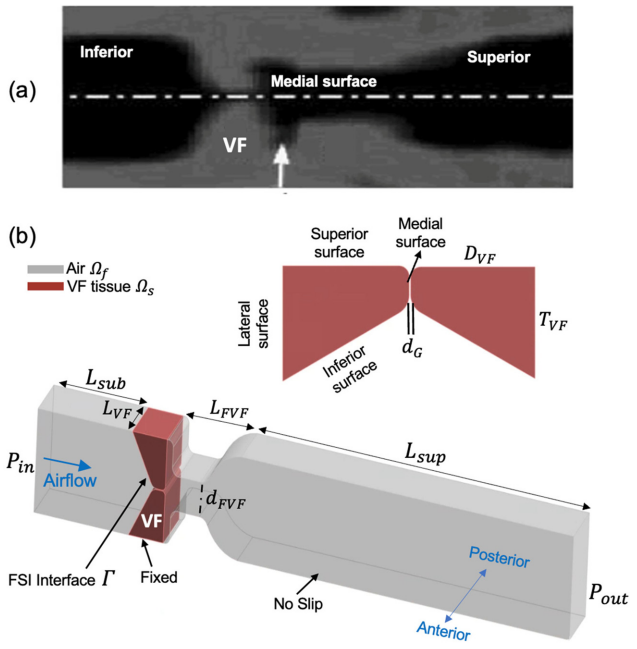

FIG. 2. (a) A close-up coronal view of the CT at the anterior–posterior midline of the glottis adapted with permission from Zheng *et al.*, Ann. Biomed. Eng. **37**(3), 625–642 (2009).[24] Copyright 2009 Published by Springer Nature, with the central line shown with white dash-dotted line. (b) The geometric model of the idealized three-dimensional glottal airflow Ω_f and VF Ω_s domains that attempts to match the key geometrical features in the CT scan. The inlet, outlet, FSI interface Γ, and various geometrical dimensions are identified.

TABLE I. Geometric modeling parameters and their related values.

Geometric parameter	Value (cm)
Minimum glottal gap width d_G	0.02
Subglottal distance L_{sub}	3.0
Supraglottal distance L_{sup}	10.5
False vocal folds width L_{FVF}	0.82
False vocal folds distance d_{FVF}	1.1
Length of vocal folds L_{VF}	0.9[4,37]–1.5[38,39]
Baseline length	1.2
Thickness of vocal folds T_{VF}	0.5[40]–1.1[4]
Baseline thickness	0.8
Depth of vocal folds D_{VF}	0.5[40]–1.2[41]
Baseline depth	0.86

defined and attempts to match the key geometrical features in the CT image. The shortest distance between the two VFs along the medial surfaces is time-varying during the VF deformation and is defined as the glottal gap, denoted by d_G. A small threshold of 0.02 cm is enforced for the minimum glottal gap between the two folds, which is in the range reported by Fulcher and Scherer[29] and has been used in previous phonation models.[30] Imposing this gap instead of a complete glottal closure is necessary to prevent the flow domain from being disconnected during the VF closure and to ensure the success of the flow solver.[31]

Table I contains the geometric dimensions of the larynx domain and the range of gender-specific anatomical measurements of VFs derived from collective data of previous studies. The geometric parameters include the length (L_{VF}), thickness (T_{VF}), and depth (D_{VF}) of the VFs, as defined in Sec. II A. Table I also provides dimensions of the baseline larynx model as displayed in Figs. 2 and 3. This geometry is comparable with the widely used simplified M5 model proposed by Thomson *et al.* and Scherer *et al.*[32,33] and also corresponds to the larynx model in Ref. 34.

A. Geometrical models: Parametric space of VFs

Nine three-dimensional geometries of the VFs in the larynx are created according to gender-related geometrical parameters, characterized by a variation in VF length L_{VF}, thickness T_{VF}, and depth D_{VF} for each case. The cubic visualization of the parametric space, where each

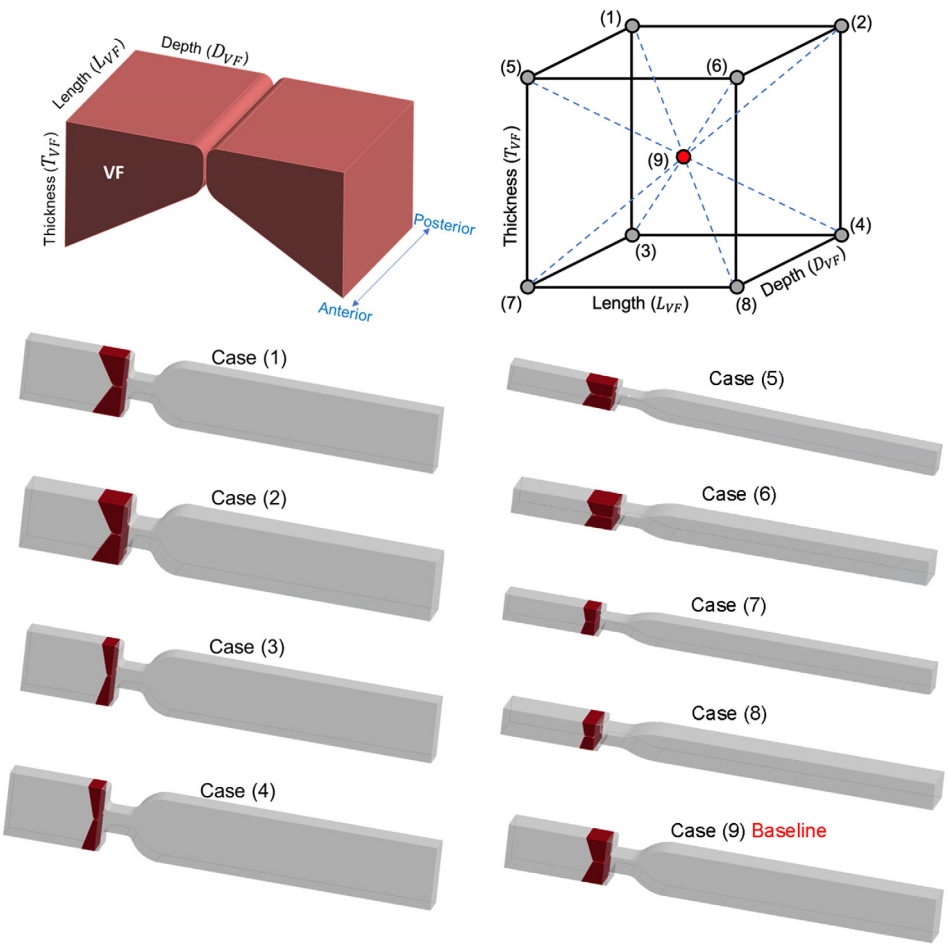

FIG 3. Top: an illustration of the vocal fold component highlighting the key geometrical parameters under investigation in the study and the explored parametric space for geometric control of the VF model with case identifications clarified at the corners. Bottom: the nine three dimensional laryngeal models, representative of females' and males' geometries. In each plotted image, larynx is colored in gray and VF domain is depicted in red.

point represents one of the nine larynx-VF geometries used in this study, along with their model schematics is displayed in Fig. 3. The VF length L_{VF} is defined as the anterior–posterior distance across the VF, with the thickness variable T_{VF} on the lateral surface in the vertical direction. Each fold tapers toward the medial direction with the reduced thickness at its medial surface. The VFs extend by the medial–lateral depth of D_{VF} toward the glottal midline in the coronal cross section. The values of these parameters used to design the laryngeal-VF models for each case are listed in Table II. In particular, each parameter varied between two chosen values based on the upper and lower range for male and female morphological data as provided in Table I. These dimensions are selected as close as possible to data reported in previous studies.[4,35,36]

The 3D parametric space shown in Fig. 3 is divided into two 2D planes that partition cases by D_{VF} values to simulate small and large laryngeal domains. Cases 1–4 correspond to $D_{VF} = 1.2$ cm, while cases 5–8 represent $D_{VF} = 0.5$ cm. VF depth D_{VF} is kept constant for each laryngeal model size, and the VF thickness and VF length are varied to create two groups of four VF cases. The VF length and thickness vary on the values of $L_{VF} = 0.9$, 1.5 cm and $T_{VF} = 0.5$, 1.1 cm, respectively. Thus, the analysis accounts for the combination of "short/long" and "thin/thick" VFs in "small/large" laryngeal models. The resulting eight cases are representative of female-like and male-like larynx models, with the condition of short-thin VF geometries for females vs long-thick geometries for males. The red point located in the center of the parametric space (Fig. 3) is the baseline case, which represents the average dimensions for each parameter. The glottal gap between the VFs, and the subglottal and supraglottal lengths of the airflow domain are kept constant for all the analyzed cases.

B. Governing equations: Glottal aerodynamics and VF dynamics

The unsteady, viscous, incompressible Navier–Stokes equations governing the glottal airflow is defined in a deformable domain $\Omega_f(t)$, consisting of the momentum and mass conservation equations as follows:

$$\rho_f\left(\frac{\partial \boldsymbol{v}}{\partial t} + \boldsymbol{v}\cdot\nabla\boldsymbol{v}\right) = \nabla\cdot\boldsymbol{\sigma_f} \quad \text{in } \Omega_f(t), \tag{1}$$

$$\nabla\cdot\boldsymbol{v} = 0 \quad \text{in } \Omega_f(t). \tag{2}$$

TABLE II. Parameters of VF geometry for each larynx model.

Case ID	Length L_{VF} (m)	Thickness T_{VF} (m)	Depth D_{VF} (m)
Case (1)	0.9×10^{-2}	1.1×10^{-2}	1.2×10^{-2}
Case (2)	1.5×10^{-2}	1.1×10^{-2}	1.2×10^{-2}
Case (3)	0.9×10^{-2}	0.5×10^{-2}	1.2×10^{-2}
Case (4)	1.5×10^{-2}	0.5×10^{-2}	1.2×10^{-2}
Case (5)	0.9×10^{-2}	1.1×10^{-2}	0.5×10^{-2}
Case (6)	1.5×10^{-2}	1.1×10^{-2}	0.5×10^{-2}
Case (7)	0.9×10^{-2}	0.5×10^{-2}	0.5×10^{-2}
Case (8)	1.5×10^{-2}	0.5×10^{-2}	0.5×10^{-2}
Case (9) baseline	1.2×10^{-2}	0.8×10^{-2}	0.86×10^{-2}

Here, $\boldsymbol{v}$ and ρ_f represent the fluid velocity field in the larynx and air density, respectively, and $\boldsymbol{\sigma_f} = -p_f\boldsymbol{I} + 2\mu_f\boldsymbol{D}(\boldsymbol{v})$ stands for the fluid Cauchy stress tensor where p_f is fluid pressure and μ_f denotes air dynamic viscosity. The symmetric part of fluid velocity gradient is defined as $\boldsymbol{D}(\boldsymbol{v}) = \frac{1}{2}(\nabla\boldsymbol{v} + \nabla\boldsymbol{v}^T)$. The airflow in the larynx can be regarded as incompressible Newtonian fluid for low Mach numbers (Ma < 0.3), as is the case in human phonation. Therefore, the fluid is assumed to have the constant density of $\rho_f = 1.185\,\text{kg/m}^3$ and viscosity of $\mu_f = 1.831\times10^{-5}\,\text{kg/m s}$, representing airflow properties at 25 °C room temperature. The flow is also considered to be laminar based on the computed Reynolds numbers in Sec. II C, and similar to many previous models, which has been found to provide reasonable approximation for laryngeal flow (see Ref. 17 for detailed discussions).

The VF tissue is assumed to be homogeneous, incompressible, and isotropic; and its deformation is modeled using the momentum equation for balance of total force:

$$\rho_s\frac{D^2\boldsymbol{U}}{Dt^2} - \nabla\cdot(\boldsymbol{\sigma}_s) = 0 \quad \text{in } \Omega_s(t). \tag{3}$$

In Eq. (3), ρ_s is the VF density and $\boldsymbol{\sigma}_s$ denotes the Cauchy stress tensor and includes the displacement $\boldsymbol{U}$, for which the elastic behavior is modeled to be linear. The density of $\rho_s = 1070\,\text{kg/m}^3$ is considered. The elasticity stress tensor for the VF tissue is defined as

$$\boldsymbol{\sigma}_s = \frac{E_s}{1+\mu_s}D(\boldsymbol{U}) + \frac{E_s\,\mu_s}{(1+\mu_s)(1-2\mu_s)}(\nabla\cdot\boldsymbol{U})\,\boldsymbol{I}. \tag{4}$$

In Eq. (4), E_s and μ_s are the Young's modulus and the Poisson's ratio of the tissue. These stiffness parameters are considered to be $E_s = 40$ kPa and $\mu_s = 0.45$, similar to previous studies,[26,42–44] and experimental measurement.[45] The symmetric part of deformation gradient for the VF tissue is denoted by $D(\boldsymbol{U}) = \frac{1}{2}(\nabla\boldsymbol{U} + \nabla\boldsymbol{U}^T)$ under the assumption of small deformations. It should be noted that considering the VF as a one-layer isotropic, linear elastic material is a common simplifying assumption in models of air flow and VF tissue interaction.[30,46,47] Justification for linear analysis has been elaborated in Ref. 48 and it has been claimed that during phonation VFs exhibit a nearly linear stress–strain relationship when active muscular tension is present.[49] Moreover, although the VF is physiologically a multilayered structure, it has been shown to behave mechanically as a one-layer structure for most phonation conditions.[50]

C. Modeling details: Fluid flow–tissue interactions and boundary conditions

Dirichlet boundary conditions are applied for the pressure at the inlet and outlet of the fluid domain, with values consistent with physiologically realistic measurements by Holmberg *et al.*[51] The subglottal pressure is identified with $P_{in} = 1$ kPa, while the gauge pressure at the outlet of supraglottal is fixed at $P_{out} = 0$ kPa. A zero normal velocity gradient condition is applied at the inflow and outflow which allows the flow rate to settle to a value dictated by the pressure drop and the flow impedance. All other bounding surfaces of the fluid domain except for the inlet and outlet are treated with no-slip and no-penetration conditions. Surfaces of the VFs in contact with air are free to move, while other boundaries are fixed. More precisely, a fixed boundary condition is applied to the VF lateral, anterior, and posterior surfaces that are in contact with the arytenoid cartilage. The

interaction between the tissue and the airflow happens along the VF superior, medial, and inferior surfaces identified by FSI interface Γ as shown in Fig. 2, and FSI coupling conditions are enforced on these common flow–tissue interfaces.

The parameters, conditions, and equations listed in Secs. II A–II C are implemented in ANSYS Workbench (version 2022.R2, ANSYS Inc., Canonsburg, PA, USA) software to carry out the fully coupled transient FSI simulations. Aerodynamics is simulated using the CFD software package in the ANSYS CFX component to capture the velocity and pressure of the air traveling through the larynx and between the VFs, while the structural deformations of the VF tissue during phonation are modeled in the ANSYS Mechanical component. Airflow dynamics and VF structural mechanics interact via a single fluid–solid coupling interface, whose behavior is dictated by the ANSYS System Coupling module, verified and validated in Ref. 52.

The Navier–Stokes and continuity equations governing the unsteady glottal airflow are numerically solved in CFX using the finite volume method, while the finite element method (FEM) is used to solve the tissue deformation equations in the Mechanical solver. Two data transfers are considered for the two-way FSI analysis: the first one is responsible to transfer the fluid force data from the CFD solver at the common air flow-VF tissue interface region to the fluid–solid interface region of the mechanical solver. The second data transfer is for transferring the incremental displacement at the fluid solid interface region in the mechanical system to the air domain as mesh displacement in the CFD system. The ANSYS System Coupling component controls the execution and convergence of fluid and solid simulations and solves fluid flow field and solid structure domains separately and in a sequential fashion. In particular, the module first performs the airflow simulations in ANSYS CFX to the target residual convergence to obtain the non-uniform pressure distribution and flow velocity in the larynx and provide the fluid forces exerted on the FSI interface. The obtained pressure load is then transferred to ANSYS Mechanical to solve for corresponding deformations of VF tissue and obtain a converged solution of the displacement data. The obtained displacements are transferred back to the CFX module, and the problem is solved for convergence. The process is iterated for the number of defined coupling iterations till the completion of all the coupling steps. The maximum number of iterations per time step was set to 10 to ensure convergence within each time step. The coupling iterations are repeated until the convergence is reached, i.e., the interactions between fluid and structural components are converged. In System Coupling, a maximum root mean square residual of 0.01 must be reached to ensure the convergence of the solution of the coupled algorithm. These stagger iterations are reinitialized with the new deformed mesh that occurs from the solid deformation. The CFX module performs mesh deformation by solving a displacement diffusion equation to determine the mesh displacements throughout the remaining volume of the mesh. In particular, a locally increasing mesh stiffness (that is, the diffusivity for the mesh displacement equation) approach is used to provide additional control over the resulting mesh distribution and to avoid mesh folding and maintain an acceptable mesh quality in regions of large deformation. The existing solution will be interpolated to the updated mesh using tools provided with the ANSYS-CFX product.

As for the FSI boundary conditions, it is assumed that the displacement of the interface Γ is the same for the fluid and solid domains which indicates that the fluid adheres to the structure. Moreover, normal stress equilibrium conditions are assumed at the FSI surfaces. These prescribed coupling conditions for the continuity of velocities and the continuity of fluid and VF tissue stresses in the normal direction are controlled by the System Coupling data transfers. In particular, to satisfy the aforementioned FSI coupling conditions across Γ, data exchange is performed at the start of every coupling iteration within a coupling step. The process is handled with the Conservative Profile Preserving data transfer algorithm and General Grid Interface (GGI) mapping algorithm is used to generate mapping weights when transferring fluid and VF tissue stresses and the resulting forces over the FSI boundary. Moreover, the Profile Preserving algorithm and the Bucket Surface mapping algorithm is used to generate mapping weights when transferring displacements along the interface between the glottal airflow and VF domains. The coupling box also manages incompatible meshes at the fluid–structure interface.

The convergence criteria of the ANSYS CFX are chosen to 10^{-5} for the normalized residuals of the global linear system of equations for the mass and momentum. The convective term in the Navier–Stokes equations is linearized by the Picard iterations and the pressure variable is evaluated at the same nodes of the velocity. The Laplace operator in the momentum equations of the airflow domain is approximated by a centered scheme, and a second-order upwind scheme is applied for spatial discretization of the convective terms. The system is then solved using an algebraic multigrid method exploiting incomplete LU factorization as smoother. The DNS (direct numerical simulation) method for laminar flow is employed. The Reynolds number for various cases is estimated to be in the range of 1300–3300 based on the maximum intraglottal velocity of 30–40 m/s and the maximum glottal gap of 0.5–1.6 mm during the VF opening phase as the characteristic length[31] and is within the realistic range for Reynolds numbers in airflow past VFs obtained in previous computational[53] and experimental[54] studies.

The nine cases are discretized into unstructured linear tetrahedral elements within the larynx and VF regions in order to perform the simulations. The computational grid for each case, including both air lumen and two vocal folds, is selected after a mesh refinement study. This is accomplished by increasing the number of elements and conducting the simulations with refined grid density until the recalculated model predictions agreed well with that from the original mesh. The resolution is considered sufficient for VF region when the maximum VF displacement does not change appreciably (relative error less than 5%), and displacement analysis with coarser and finer meshes shows negligible error (less than 3.3%) when monitoring and comparing the difference between maximum values of glottal gap width and the total displacement patterns at some examined points. The fluid flow solution is also considered mesh-independent for an error lower than 5% in terms of velocity and pressure in the glottis.

The selected final mesh for the baseline case model is split into 1.2×10^6 tetrahedral elements within the larynx and VF regions. All the simulations are performed on a non-uniform grid which provides a higher resolution in the intraglottal region where high flow gradients are expected, as well as finer meshes in the groove areas and near the FSI interface of the VFs (around the VFs domain). A coarser mesh is used at the subglottal and supraglottal regions, decreasing the computation time and required resources. In most regions, the element size is 0.3 to 0.5 mm. Moreover, different size time-steps are adopted to

comply with the Cauchy–Freidrich–Lewey (CFL) numerical stability constraint and to provide adequate temporal resolution. A time step size of $\Delta t = 10^{-5}$ s is applied on both the flow solver and the solid solver for all the cases, which is deemed to provide a good temporal resolution and an acceptable maximum CFL number with the optimal balance between computational efficiency and accuracy. Time integration was performed using an implicit second-order discretization scheme. Simulations are carried out whereby cases reached a well-defined state, such that the flow field is fully developed, and the VFs vibrate periodically.

III. RESULTS

In this section, first the results of the baseline simulation (see Table II for geometrical details) are presented. Next, the dependence of glottal aerodynamics and mechanical deformations on the variation of VF geometrical features; VF depth D_{VF}, thickness T_{VF}, and length L_{VF}; that is linked to gender-related parameters are investigated.

A. Glottal aerodynamics and tissue deformation: Baseline VF geometry

The results for laryngeal aerodynamics, including glottal flow velocity magnitude, pressure field and streamline pattern for baseline case, are shown in Fig. 4. The contours are displayed in the midcoronal and midsagittal planes at the same time instance that corresponds to the opening phase of VF in the oscillation cycle. The airflow is driven from left (inlet) to right (outlet) by a constant pressure drop between the subglottal and supraglottal pressures and interacts with the VFs to initiate flow-induced vibrations. Due to the reduction in the area available for the flow in the glottic area, a pressure drop in the larynx across the glottis occurs. This narrowing, therefore, generates a considerable increase in intra-glottal air velocity, with maximum values observed in the glottis. Figure 4 also displays the streamline structures in the airway. The uniform streamlines at the inlet form a glottal jet between the folds, then recirculate before exiting the outlet. Two vortices are observed above the glottis and persisted a short distance into the supraglottal region. Results also suggest that supraglottal velocity is highly spatial with strong recirculation zones and is temporally dependent.

The spatiotemporal VF tissue deformations of the baseline case are illustrated in Fig. 5. Snapshots are obtained from opening to fully opened, then to a closed position. The T_4 and T_7 time instants are the extreme positions of the VF when it deforms toward the superior direction and when it closes the glottis, respectively. The first row shows the profile of the VFs at the midcoronal plane, and the second row shows the superior view. As air flows through between the VFs, a rhythmic vibration is observed. The subglottal pressure produces a pushing force in the flow direction on the VFs as well as a compressive force in the transverse direction, causing both inferior and superior surfaces to abduct, and the glottis begins to open. The opening arrives at the maximum level and then adducting starts from the inferior area followed by the superior area. Then, the VFs begin closing and the cycle is repeated (Fig. 5).

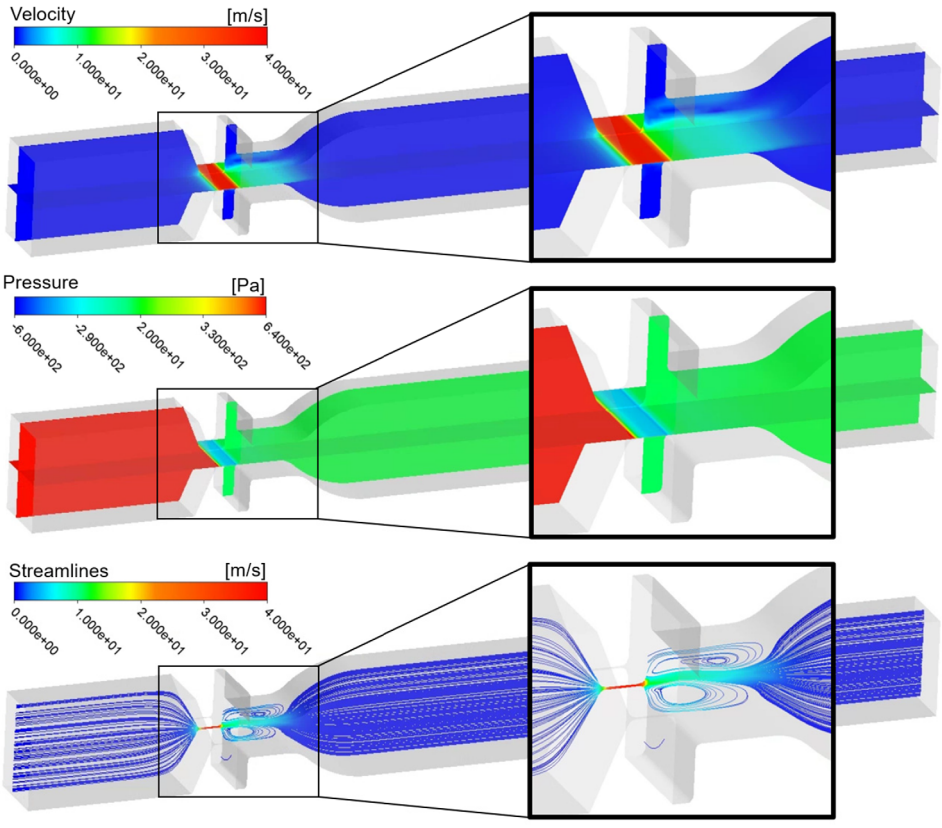

FIG. 4. Contours of velocity field, pressure, and velocity surface streamlines in the midcoronal and midsagittal plane in the larynx domain captured during glottal opening time instant. The box shows a zoomed part of the plot to observe the aerodynamics in the glottal region.

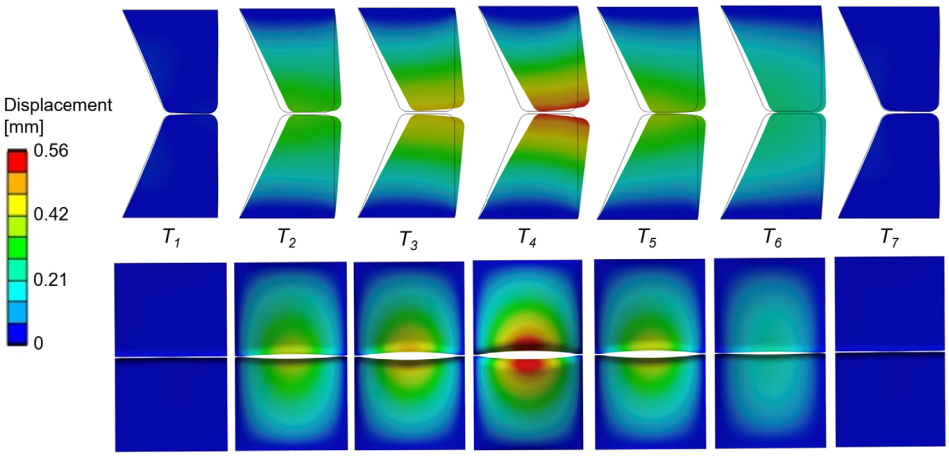

FIG. 5. A series of deformed VF surface shapes (coronal and axial views) within a phonation cycle shifted in the horizontal direction for $P_{in} = 1$ kPa and baseline case. The solid black curves are the undeformed positions of the folds.

B. Effect of morphological differences: Nine VF geometries

In this section, the results from nine laryngeal models are described. Figure 6 shows a comparison of pressure decrease across the glottis and flow rate chart for cases with various VF morphologies. In both Fig. 6 plots, the red color represents the baseline case information. The intra-glottal pressure is obtained for these cases on the centerline of the larynx, only in the portion that passes through the glottis where VF is located. Also, the glottal flow rate is captured on a plane that is located at the middle portion of the larynx geometry, when velocity is the maximum.

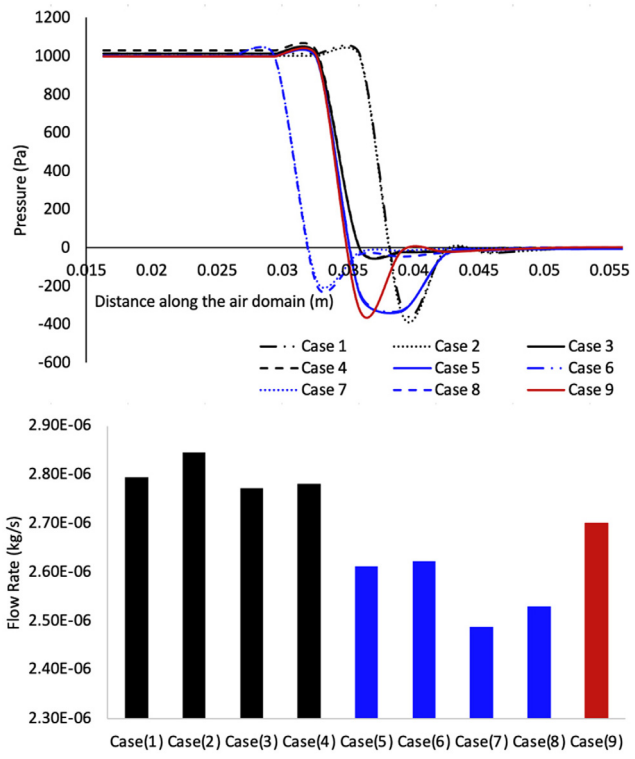

FIG. 6. Top: comparison of the intraglottal airflow pressure along the axial length of the glottal region in nine VF cases. Bottom: comparison of the maximum flow rate within the glottis in the same cases.

It can be observed that the intra-glottal pressures decrease for all the configurations as the glottal cross-sectional area decreases due to flow acceleration within the glottis (Fig. 6). This pressure reduction reaches minimum values (and the largest velocities) just past the minimum diameter position, and then the glottal pressure increases as the cross-sectional area expands at the supraglottal area. Figure 6 shows that intraglottal pressure patterns are similar and the differences in pressure distributions between all configurations are relatively small. Compared to the other cases studied here, case 2 gives the lowest dip in pressure and the greatest flow rate, which suggests that this case corresponds to the least flow resistance.

By comparing the cases with different thickness T_{VF}, but same L_{VF} and D_{VF} (i.e., case 2 vs case 4), it can be observed that the effect of thickness on pressure drop is noticeable. The thicker the VF, the bigger the pressure drop, and a higher flow rate is obtained. By comparing the cases with different length L_{VF}, but same D_{VF} and T_{VF} (i.e., case 1 vs case 2), the calculated pressure drop is found to be independent of the change of the VF length; however, the flow rate consistently increases for the cases with a longer VF due to a bigger cross-sectional area of the glottal region. For the cases with smaller VF depth D_{VF}, but same L_{VF} and T_{VF} (cases 5–8 appeared by blue vs cases 1–4 presented by black color in Fig. 6), the pressure drop happens sooner in the subglottal length, and the flow rate is consistently lower because of the smaller cross-sectional area of glottis.

Moreover, the contour of the total displacement of nine VF cases is shown in Fig. 7, taken when the glottal flow rate has its maximum value. The VF length L_{VF} shows a detectable effect on the tissue deformation followed by VF thickness T_{VF}. Increasing L_{VF} increases the maximum displacement significantly. This is consistently observed by increasing the length from cases 1, 3, 5, and 7 that have the L_{VF} of 0.9 cm to cases 2, 4, 6, and 8 with the L_{VF} of 1.5 cm. On the other hand, decreasing VF thickness T_{VF} increases displacement remarkably as well in all the pairs with same VF length and depth. Finally, decreasing depth D_{VF} from 1.2 cm in Cases 1, 2, 3, and 4 to 0.5 cm in cases 5,

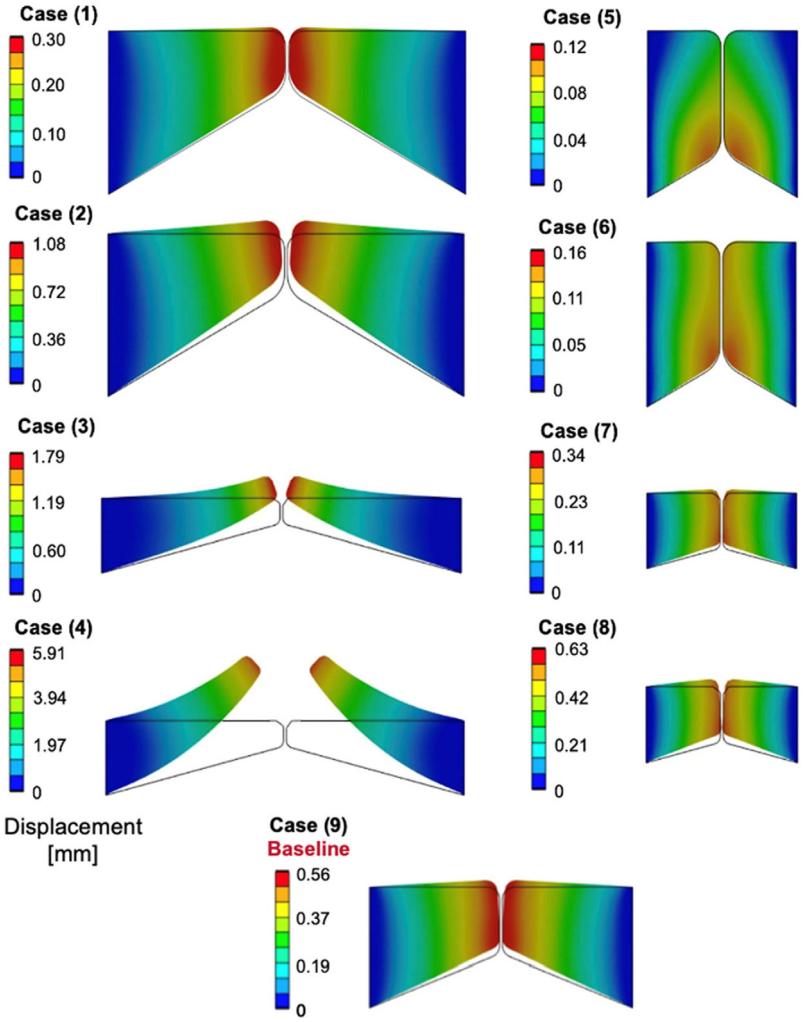

FIG. 7. Comparison of the deformation contours for nine VF cases taken at opening of glottis when the glottal flow has its maximum value. The values of the total displacements of the VFs in millimeter are indicated by different color contours.

6, 7, and 8 decreases maximum displacement between all the case pairs with the same VF length and thickness.

Figure 8 demonstrates the maximum VF deformation during vibration for the nine analyzed models, using different subglottal pressure values. The inlet pressure P_{in} varied for three phonation loads between 0.8 and 1.5 kPa, which covers the range in normal phonation conditions and the highest VF displacement is calculated at each subglottal pressure. As P_{in} was raised from 0.8 to 1.5 kPa, the deformation of VF increased as expected. The vibration magnitude shows a linear relationship with inlet pressure. More precisely, the data collected for the variation of maximum VF displacement vs inlet lung pressure for each of the presented cases collapsed onto a single line (Fig. 8). Therefore, data have been fitted using a linear function that has the form of $y = mx + b$, where (m) is the slope that quantifies the sensitivity of the deformation of the VF (y) with respect to the subglottal pressure (x) and (b) is the y intercept. We observe that the slope of the lines is different for each case. In particular, m for the case 3 (thin-short VF) and the case 2 (thick-long VF) have the largest values (Fig. 8). Therefore, the subglottal pressure was found to have maximal effect

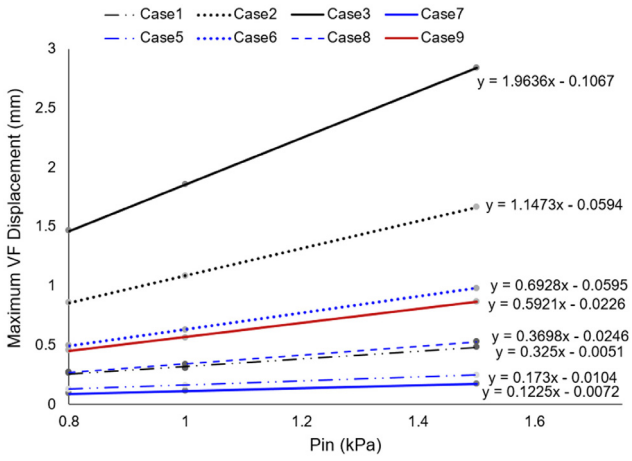

FIG. 8. Effect of subglottal pressure on maximum VF displacement. Case 4 has a larger displacement and is not included.

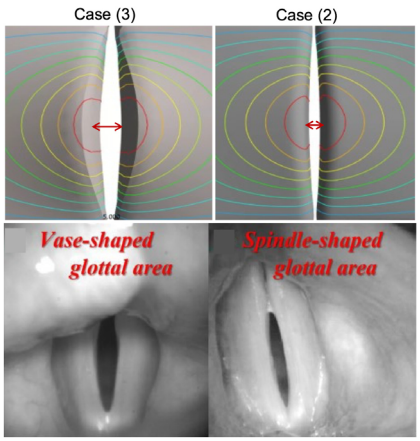

FIG. 9. Comparison of the glottis region from FSI simulation (superior view) with clinical examples of the glottal configuration for males and females adapted with permission from Yamauchi *et al.*, J. Voice **28**(5), 525–531 (2014).[55] Copyright 2014 The Voice Foundation, Published by Elsevier Inc.

on VF displacement in these cases. The shape of the glottal configuration between these aforementioned cases is compared in Fig. 9. It demonstrates case 2 with the long-thick VFs and case 3 with the short-thin VFs, representative of male-like and female-like VF geometries, respectively. The glottal area of case 3 has an hourglass shape, while case 2 is spindle-shaped.

Table III compares female-like (case 3) and male-like (case 2) VF models in terms of the parameters of voice production, namely, vibration and glottal gap dynamics. The vibration frequency is evaluated by plotting the variations of maximum VF displacement vs time for the aforementioned models (Fig. 10) and indicates values of 106.3 Hz for the long-thick VF and 152.1 Hz for the short-thin cases, respectively. As can be seen from Fig. 10, both cases have reached a stationary state wherein the maximum displacement and, therefore, maximum glottal gap is nearly constant from cycle-to-cycle for the two cases.

The qualitative studies of the cases 2 and 3 models show that VF geometric parameters have an influence on vibration frequency. In particular, decreasing the length and thickness of the VF in case 3 in comparison to case 2 increases the calculated phonation frequency from the variation in Fig. 10. It should be mentioned that the vibration frequency of both models is in the natural range of human voice production. By comparing the maximum values of glottal gap in both models, it can be observed that the glottal gap opening in case 2 is greater than the case 3 VF along with the vibration cycle which affects the value of volume flux.

IV. DISCUSSION

The objective of this study is to investigate the relationship between the geometrical sizes of the human VFs associated with gender, and the

TABLE III. Comparison of flow parameters obtained for cases 2 and 3.

Parameter	Case 3	Case 2
Vibration frequency (Hz)	152.1	106.3
Maximum glottal gap (mm)	1.1	1.6

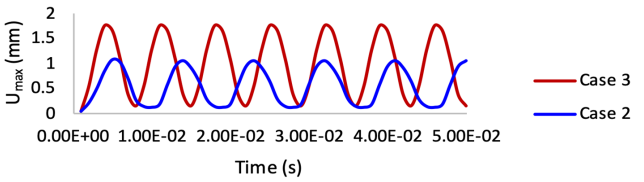

FIG. 10. Time variations of maximum VF displacement values for cases 2 and 3 models displayed in Fig. 9.

airflow-VF interactions during phonation. Particularly, it demonstrates how physiologically meaningful variations in VF geometric parameters affect the model outcome, thereby providing future simulations with important information on the respective parametric sensitivities. Nine different geometries are simulated and compared. The results show that the model is capable of reproducing the aerodynamic data through the larynx with a good approximant. In particular, the obtained pressure drops across the glottis and flow fields (Fig. 4), as well as the flow rates (Fig. 6), are consistent with CFD data published previously[22,56] and experimental recording of glottal airflow.[51] Furthermore, obtained VF displacements agree well with previous studies using simplified VF geometry.[22,30,57] The deformations from the baseline model are matched reasonably well with.[24] Although the model was able to produce vibration patterns and flow characteristics similar to what has been reported in humans, it should be noted that validation compared to experiments is difficult due to the lack of reliable methods for measurement of the material properties and geometry, which indicates most of the model input parameters have to be estimated, preventing direct quantitative validation.

The results showed that the differences in VF length and thickness have opposite effects on the tissue's biomechanical response. Specifically, while the longer VFs increased the tissue displacement and glottal flow, the larger thickness had an effect of significantly reducing the maximum VF vibration amplitude, consistent with observations in Zhang *et al.*[26] Highest VF displacement of a few millimeters is obtained for the thinnest and longest VF in case 4 (Fig. 7) while varying VF length across all the cases is noted to affect the displacement directly when thickness and depth are held constant. This pattern is observed regardless of inlet pressure as illustrated in Fig. 8. Conversely, increasing VF thickness causes both the glottal pressure drop and the flow rate to increase. The smaller thickness results in lower pressures within the glottis compared to thick VF, with consequentially less force to separate the VFs during glottal opening and smaller flow rate (see Fig. 6). Therefore, thicker and longer VF causes higher flow rate, as also pointed out previously by Li *et al.*[27] Additionally, smaller VF depth is found to be associated with smaller flow rate and tissue deformation due to smaller laryngeal size, which decreases the cross-sectional area of the glottis and thus increases the airflow resistances in small depth configurations for the same transglottal pressure (Fig. 6). These findings are consistent with observations in the previous study by Li *et al.*[27] and the clinical recordings of glottal airflow in Ref. 58 that found higher transglottal airflow in males, that usually have long-thick VFs in the larger larynx. We also observed that airflow velocities in the models with thin and short VFs are similar in value to the velocities in the thick and long ones, thus seemingly identical aerodynamics would lead to different VF deformations in different larynges. A comparison of glottal area for two selected cases (Fig. 9) with high-speed digital images in Ref. 55

confirms the accurate representation of the glottal configuration. A vase-shaped configuration with a slightly curved edge is observed for short-thin VF (case 3), which has been frequently shown by females. The long-thick VF (case 2) had a spindle-shaped glottal configuration with a straight margin that is often observed in males.[55] Finally, the obtained linear relationship between the vibration magnitude and the subglottal pressure is consistent with previous numerical findings[59] for the similar range of lung pressure used in the current study.

As discussed earlier, following the approach taken in the vast majority of past studies, an idealized model of the larynx is employed. While this parametrically controlled geometry helps in controlling the effect of each geometrical feature investigating its contribution, subject-specific sets of glottal geometries based on the magnetic resonance scan that compare the female and male larynx is necessary to establish models that predict the phonation conditions that are benign to voice health. In addition to using patient-specific models, in order to make this computational model functional in clinical setting and investigate the prevalence of certain voice disorder in genders, the frequency analysis of VF vibration and the resulting acoustic measures need to be incorporated within the framework to comprehensively analyze the relationship between VF morphology and the vibration mode, which can be the subject of future research.

Another limitation is the imposed artificial gap between the two folds, allowing leakage flow even during what would be considered a glottal closure. Furthermore, the laminar flow for laryngeal models is considered. The majority of previous studies found that the Reynolds numbers in airflow in the larynx range from 1000 to 5000.[54] While the subglottal flow may be laminar, near the glottal region the transition to turbulent flow occurs. The comprehensive investigations of intraglottal flow have revealed complex flow patterns and morphologies[60] characterized by features such as transition to turbulence and the corresponding flow structure[61] and the numerical computation of this highly unsteady airflow with massive separation is the focus of future studies. Moreover, in this work, the VF is treated as an impermeable single-phase structure. While this is a common assumption in all the previous FSI simulations of phonation due to significant complexity of incorporating a biphasic VF[62] models, the 80% fluid volume fraction of the VF tissue justifies the use of a permeable material.[63] Hence, future work extends this study to model the VF tissue as a porous medium similar to our previous fluid–porous structure framework[64,65] and explore the flow within the folds combined with oxygen transport[66,67] which can also provide additional information on VF hydration.[68] In addition, simulations are performed for a limited number of values for each geometrical parameter to represent the morphological differences between female-like and male-like VF. Although the results of nine larynx models support the important role of the VF shape on its biomechanics, it would be ideal to consider a wider range of possible geometries to reach stronger conclusions. The VF tissue is assumed to be homogeneous and isotropic, while experimental evidence suggests that VF is an anisotropic material. This can affect the realistic dynamics of VFs during the closing phase and the degree of error introduced by this assumption will be investigated in future studies. However, it should be noted that the values of the comparative results in the VF opening phase are still valid, and for a parametric study such as presented here, limiting the focus to an isotropic VF would not alter the current conclusions.

ACKNOWLEDGMENTS

This project was funded by the Charles Henry Leach II Fund and the National Science Foundation under Grant No. CBET 2138225.

AUTHOR DECLARATIONS

Conflict of Interest

The authors have no conflicts to disclose.

Author Contributions

Alexis Throop and Durwash Badr contributed equally to this work.

Isabella McCollum: Data curation (lead); Formal analysis (equal); Visualization (lead); Writing – original draft (equal). **Alexis Throop:** Data curation (equal); Visualization (equal). **Durwash Badr:** Data curation (equal); Visualization (equal). **Rana Zakerzadeh:** Conceptualization (lead); Formal analysis (equal); Funding acquisition (lead); Methodology (lead); Project administration (lead); Supervision (lead); Writing – original draft (equal).

DATA AVAILABILITY

The data that support the findings of this study are available from the corresponding author upon reasonable request.

REFERENCES

[1]I. R. Titze, "The physics of small-amplitude oscillation of the vocal folds," J. Acoust. Soc. Am. **83**(4), 1536–1552 (1988).
[2]E. Van Houtte, K. Van Lierde, E. D'haeseleer, and S. Claeys, "The prevalence of laryngeal pathology in a treatment-seeking population with dysphonia," Laryngoscope **120**(2), 306–312 (2010).
[3]R. Mittal, B. D. Erath, and M. W. Plesniak, "Fluid dynamics of human phonation and speech," Annu. Rev. Fluid Mech. **45**(1), 437–467 (2013).
[4]I. R. Titze, "Physiologic and acoustic differences between male and female voices," J. Acoust. Soc. Am. **85**(4), 1699–1707 (1989).
[5]I. R. Titze, "Physiology of the female larynx," J. Acoust. Soc. Am. **82**(S1), S90–S91 (1987).
[6]D. A. Puts, C. L. Apicella, and R. A. Cárdenas, "Masculine voices signal men's threat potential in forager and industrial societies," Proc. R Soc. B **279**(1728), 601–609 (2012).
[7]P. H. Dejonckere, *Occupational Voice: Care and Cure* (Kugler Publications, 2001).
[8]E. J. Hunter, K. Tanner, and M. E. Smith, "Gender differences affecting vocal health of women in vocally demanding careers," Logop., Phoniatr., Vocology **36**(3), 128–136 (2011).
[9]S. N. Awan and J. A. Awan, "The effect of gender on measures of electroglottographic contact quotient," J. Voice **27**(4), 433–440 (2013).
[10]N. Roy, R. M. Merrill, S. Thibeault, R. A. Parsa, S. D. Gray, and E. M. Smith, "Prevalence of voice disorders in teachers and the general population," J. Speech Lang. Hear. Res. **47**, 281–293 (2004).
[11]S. Thomson, J. Tack, and G. Verkerke, "A numerical study of the flow-induced vibration characteristics of a voice-producing element for laryngectomized patients," J. Biomech. **40**(16), 3598–3606 (2007).
[12]S. Kosako, M. Hiramatsu, Y. Fujimoto, and Y. Tsuji, "Downstream flow field structure in voice prosthesis and its effect on sound generation around the esophageal wall," Phys. Fluids **35**, 025114 (2023).
[13]N. P. Solomon, L. E. Glaze, R. R. Arnold, and M. van Mersbergen, "Effects of a vocally fatiguing task and systemic hydration on men's voices," J. Voice **17**(1), 31–46 (2003).
[14]M. P. Gelfer, M. L. Andrews, and C. P. Schmidt, "Effects of prolonged loud reading on selected measures of vocal function in trained and untrained singers," J. Voice **5**(2), 158–167 (1991).

[15]M. A. Nemetz, P. Pontes, V. P. Vieira, and R. K. Yazaki, "Vestibular fold configuration during phonation in adults with and without dysphonia," Rev. Bras. Otorrinolaringol. **71**, 6–12 (2005).
[16]Z. Zhang, "Mechanics of human voice production and control," J. Acoust. Soc. Am. **140**(4), 2614 (2016).
[17]P. Šidlof, J. Horáček, and V. Řidký, "Parallel CFD simulation of flow in a 3D model of vibrating human vocal folds," Comput. Fluids **80**, 290–300 (2013).
[18]D. O. Frank-Ito, K. Schulz, G. Vess, and D. L. Witsell, "Changes in aerodynamics during vocal cord dysfunction," Comput. Biol. Med. **57**, 116–122 (2015).
[19]L. T. Zhang and J. Yang, "Evaluation of aerodynamic characteristics of a coupled fluid-structure system using generalized Bernoulli's principle: An application to vocal folds vibration," J. Coupled Syst. Multiscale Dyn. **4**(4), 241–250 (2016).
[20]Q. Xue, X. Zheng, R. Mittal, and S. Bielamowicz, "Subject-specific computational modeling of human phonation," J. Acoust. Soc. Am. **135**(3), 1445–1456 (2014).
[21]S. Chang, C. K. Novaleski, T. Kojima, M. Mizuta, H. Luo, and B. Rousseau, "Subject-specific computational modeling of evoked rabbit phonation," J. Biomech. Eng. **138**(1), 011005 (2016).
[22]W. Jiang, X. Zheng, and Q. Xue, "Computational modeling of fluid-structure-acoustics interaction during voice production," Front. Bioeng. Biotechnol. **5**, 7 (2017).
[23]S. Zorner, M. Kaltenbacher, and M. Dollinger, "Investigation of prescribed movement in fluid-structure interaction simulation for the human phonation process," Comput. Fluids **86**(100), 133–140 (2013).
[24]X. Zheng, S. Bielamowicz, H. Luo, and R. Mittal, "A computational study of the effect of false vocal folds on glottal flow and vocal fold vibration during phonation," Ann. Biomed. Eng. **37**(3), 625–642 (2009).
[25]M. Döllinger, P. Gómez, R. R. Patel, C. Alexiou, C. Bohr, and A. Schützenberger, "Biomechanical simulation of vocal fold dynamics in adults based on laryngeal high-speed videoendoscopy," PLoS One **12**(11), e0187486 (2017).
[26]Z. Zhang, "Contribution of laryngeal size to differences between male and female voice production," J. Acoust. Soc. Am. **150**(6), 4511–4521 (2021).
[27]S. Li, R. C. Scherer, M. Wan, S. Wang, and B. Song, "Intraglottal pressure: A comparison between male and female larynxes," J. Voice **34**(6), 813–822 (2020).
[28]A. Lodermeyer, S. Becker, M. Döllinger, and S. Kniesburges, "Phase-locked flow field analysis in a synthetic human larynx model," Exp. Fluids **56**(4), 77 (2015).
[29]L. P. Fulcher and R. C. Scherer, "Phonation threshold pressure: Comparison of calculations and measurements taken with physical models of the vocal fold mucosa," J. Acoust. Soc. Am. **130**(3), 1597–1605 (2011).
[30]H. Luo, R. Mittal, and S. A. Bielamowicz, "Analysis of flow-structure interaction in the larynx during phonation using an immersed-boundary method," J. Acoust. Soc. Am. **126**(2), 816–824 (2009).
[31]H. Luo, R. Mittal, X. Zheng, S. A. Bielamowicz, R. J. Walsh, and J. K. Hahn, "An immersed-boundary method for flow–structure interaction in biological systems with application to phonation," J. Comput. Phys. **227**(22), 9303–9332 (2008).
[32]R. C. Scherer, D. Shinwari, K. J. De Witt, C. Zhang, B. R. Kucinschi, and A. A. Afjeh, "Intraglottal pressure profiles for a symmetric and oblique glottis with a divergence angle of 10 degrees," J. Acoust. Soc. Am. **109**(4), 1616–1630 (2001).
[33]S. L. Thomson, L. Mongeau, and S. H. Frankel, "Aerodynamic transfer of energy to the vocal folds," J. Acoust. Soc. Am. **118**(3), 1689–1700 (2005).
[34]H. Sadeghi, S. Kniesburges, M. Kaltenbacher, A. Schutzenberger, and M. Dollinger, "Computational models of laryngeal aerodynamics: Potentials and numerical costs," J. Voice **33**(4), 385–400 (2019).
[35]H. Hollien, "Vocal pitch variation related to changes in vocal fold length," J. Speech Hear. Res. **3**(2), 150–156 (1960).
[36]H. Hollien and J. F. Curtis, "A laminagraphic study of vocal pitch," J. Speech Hear. Res. **3**(4), 361–371 (1960).
[37]H. Hollien, "Vocal fold dynamics for frequency change," J. Voice **28**(4), 395–405 (2014).
[38]F. Alipour, D. A. Berry, and I. R. Titze, "A finite-element model of vocal-fold vibration," J. Acoust. Soc. Am. **108**(6), 3003–3012 (2000).
[39]J. A. X. Filho, E. C. M. de Melo, C. de Giacomo Carneiro, D. H. Tsuji, and L. U. Sennes, "Length of the human vocal folds: Proposal of mathematical equations as a function of gender and body height," Ann. Otol. Rhinol. Laryngol. **114**(5), 390–392 (2005).
[40]M. K. Mobashir, A. Mohamed, A. S. Quriba, A. M. Anany, and E. M. Hassan, "Linear measurements of vocal folds and laryngeal dimensions in freshly excised human larynges," J. Voice **32**(5), 525–528 (2018).
[41]Z. Zhang, "Cause-effect relationship between vocal fold physiology and voice production in a three-dimensional phonation model," J. Acoust. Soc. Am. **139**(4), 1493 (2016).
[42]F. Alipour and S. Vigmostad, "Measurement of vocal folds elastic properties for continuum modeling," J. Voice **26**(6), 816.e21–816.e29 (2012).
[43]F. Alipour and R. C. Scherer, "Time-dependent pressure and flow behavior of a self-oscillating laryngeal model with ventricular folds," J. Voice **29**(6), 649–659 (2015).
[44]Z. Zhang, "Estimation of vocal fold physiology from voice acoustics using machine learning," J. Acoust. Soc. Am. **147**(3), EL264 (2020).
[45]D. K. Chhetri, Z. Zhang, and J. Neubauer, "Measurement of Young's modulus of vocal folds by indentation," J. Voice **25**(1), 1–7 (2011).
[46]M. Itskov and N. Aksel, "Elastic constants and their admissible values for incompressible and slightly compressible anisotropic materials," Acta Mech. **157**(1), 81–96 (2002).
[47]Z. Zhang, "The influence of material anisotropy on vibration at onset in a three-dimensional vocal fold model," J. Acoust. Soc. Am. **135**(3), 1480–1490 (2014).
[48]D. D. Cook, E. Nauman, and L. Mongeau, "Reducing the number of vocal fold mechanical tissue properties: Evaluation of the incompressibility and planar displacement assumptions," J. Acoust. Soc. Am. **124**(6), 3888–3896 (2008).
[49]I. R. Titze and F. Alipour, *The Myoelastic Aerodynamic Theory of Phonation* (National Center for Voice and Speech, 2006).
[50]J. Yin and Z. Zhang, "The influence of thyroarytenoid and cricothyroid muscle activation on vocal fold stiffness and eigenfrequencies," J. Acoust. Soc. Am. **133**(5), 2972–2983 (2013).
[51]E. B. Holmberg, R. E. Hillman, and J. S. Perkell, "Glottal airflow and transglottal air pressure measurements for male and female speakers in low, normal, and high pitch," J. Voice **3**(4), 294–305 (1989).
[52]S. K. Chimakurthi, S. Reuss, M. Tooley, and S. Scampoli, "ANSYS Workbench system coupling: A state-of-the-art computational framework for analyzing multiphysics problems," Eng. Comput. **34**(2), 385–411 (2018).
[53]W. Jiang, C. Farbos de Luzan, X. Wang, L. Oren, S. M. Khosla, Q. Xue, and X. Zheng, "Computational modeling of voice production using excised canine larynx," J. Biomech. Eng. **144**(2), 021003 (2022).
[54]B. D. Erath and M. W. Plesniak, "An investigation of asymmetric flow features in a scaled-up driven model of the human vocal folds," Exp. Fluids **49**, 131–146 (2010).
[55]A. Yamauchi, H. Yokonishi, H. Imagawa, K.-I. Sakakibara, T. Nito, N. Tayama, and T. Yamasoba, "Age-and gender-related difference of vocal fold vibration and glottal configuration in normal speakers: Analysis with glottal area waveform," J. Voice **28**(5), 525–531 (2014).
[56]P. Nithiarasu, O. Hassan, K. Morgan, N. Weatherill, C. Fielder, H. Whittet, P. Ebden, and K. Lewis, "Steady flow through a realistic human upper airway geometry," Int. J. Numer. Methods Fluids **57**(5), 631–651 (2008).
[57]A. Vazifehdoostsaleh, N. Fatouraee, M. Navidbakhsh, and F. Izadi, "Three dimensional FSI modelling of sulcus vocalis disorders of vocal folds," J. Mech. **34**(6), 791–800 (2018).
[58]E. B. Holmberg, R. E. Hillman, and J. S. Perkell, "Glottal airflow and transglottal air pressure measurements for male and female speakers in soft, normal, and loud voice," J. Acoust. Soc. Am. **84**(2), 511–529 (1988).
[59]C. Tao, J. J. Jiang, and Y. Zhang, "Simulation of vocal fold impact pressures with a self-oscillating finite-element model," J. Acoust. Soc. Am. **119**(6), 3987–3994 (2006).
[60]T. Yoshinaga, K. Nozaki, and A. Iida, "Hysteresis of aeroacoustic sound generation in the articulation of [s]," Phys. Fluids **32**(10), 105114 (2020).
[61]T. Yoshinaga, K. Nozaki, and S. Wada, "Experimental and numerical investigation of the sound generation mechanisms of sibilant fricatives using a simplified vocal tract model," Phys. Fluids **30**(3), 035104 (2018).

[62]J. P. Noordzij and R. H. Ossoff, "Anatomy and physiology of the larynx," Otolaryngol. Clin. North Am. **39**(1), 1–10 (2006).
[63]A. K. Miri, "Mechanical characterization of vocal fold tissue: A review study," J. Voice **28**(6), 657–667 (2014).
[64]R. Zakerzadeh, T. Cupac, and M. Durka, "Oxygen transport in a permeable model of abdominal aortic aneurysm," Comput. Methods Biomech. Biomed. Eng. **24**, 215–215 (2021).
[65]A. Throop, D. Badr, M. Durka, M. Bukač, and R. Zakerzadeh, "Analyzing the effects of multi-layered porous intraluminal thrombus on oxygen flow in abdominal aortic aneurysms," Oxygen **2**(4), 518–536 (2022).
[66]B. Carbino, A. Guy, M. Durka, and R. Zakerzadeh, "The effects of geometric features of intraluminal thrombus on the vessel wall oxygen deprivation," Front. Bioeng. Biotechnol. **10**, 814995 (2022).
[67]A. Throop, M. Bukac, and R. Zakerzadeh, "Prediction of wall stress and oxygen flow in patient-specific abdominal aortic aneurysms: The role of intraluminal thrombus," Biomech. Model. Mechanobiol. **21**, 1761–1719 (2022).
[68]A. Bouvet, X. Pelorson, and A. Van Hirtum, "Airflow driven fluid–structure interaction subjected to aqueous-based liquid spraying," Phys. Fluids **32**(8), 081901 (2020).